RSC Advances

PAPER

View Article Online
View Journal | View Issue

Cite this: *RSC Adv.*, 2026, **16**, 24465

Contrasting mechanisms of UDMH degradation by MnO_2 and Mn_2O_3 under microwave assistance: electronic structure, surface adsorption and catalytic reaction pathways

Jiepeng Wang, Siyu He, Zhe Wang, Yunlong Deng, Jielei Hao, Xuqian Wang and Yongkui Zhang *

Unsymmetrical dimethylhydrazine (UDMH) is difficult to efficiently degrade and mineralize using traditional wastewater treatment processes, leading to the accumulation of toxic nitrogenous intermediates. In this study, a microwave-assisted catalytic degradation system based on manganese oxides was developed for effective UDMH treatment. Experiments were integrated with DFT calculations to systematically compare the structure–activity relationships of MnO_2 and Mn_2O_3. DFT calculations show that the metallic character of Mn_2O_3 affords high electron mobility that favors rapid reduction of intermediates, whereas semiconducting MnO_2 exhibits superior overall catalytic performance; the latter's lower oxygen-vacancy formation energy (2.10 eV *vs.* 2.41 eV) markedly decreases the barrier for the *OH → *O → *OOH sequence, intensifying oxidative pathways. DFT results, corroborated by XPS and XRD analyses, reveal that both oxides generate $^{\bullet}OH$ *via* dynamic $Mn^{4+}/Mn^{3+}/Mn^{2+}$ redox cycling and surface hydroxyl enrichment. However, MnO_2, exhibiting higher surface $^{\bullet}OH$ density and lower UDMH adsorption energy, leverages microwave-induced hot spots to sustain $^{\bullet}OH$ production, achieving >90% COD removal. Mn_2O_3 suffers from structural deactivation that constrains long-term stability. The microwave-enhanced mechanism of Mn-based catalysis was elucidated by the three-scale analysis—electronic structure, surface adsorption and catalytic reaction. This study provides a theoretical basis for the design of manganese-based catalysts and supports their applications in the microwave-assisted treatment of nitrogen-containing wastewater.

Received 3rd February 2026
Accepted 23rd April 2026

DOI: 10.1039/d6ra00930a

rsc.li/rsc-advances

1 Introduction

Unsymmetrical dimethylhydrazine (UDMH) is a high-performance rocket propellant widely applied in aerospace and other fields.[1] Although UDMH is recognized as a toxic organic pollutant possessing carcinogenic, mutagenic, teratogenic, and embryotoxic characteristics and is harmful to humans and other living organisms, it remains widely utilized due to its high specific impulse, low freezing point, and high thermal stability.[2] Once UDHM enters the environment, it causes serious pollution to soil, water and atmosphere, posing a potential threat to the ecosystem and human health. Therefore, it is of great practical significance to find an efficient and environmentally friendly UDMH degradation method.

UDMH and its degradation intermediates exhibit high biotoxicity and structural complexity; therefore, the complete degradation of UDMH is extremely challenging. Primary UDMH wastewater treatment methods include adsorption, biological degradation, and advanced oxidation processes (AOPs). While adsorption techniques[3,4] offer operational simplicity, they suffer from limited adsorption capacity, high regeneration costs, and secondary pollution risks. Biological degradation [5,6] relying on microbial metabolism, requires prolonged treatment cycles and has poor tolerance to high concentrations of UDMH. In contrast, AOPs demonstrate advantages by generating highly reactive oxidative species (*e.g.*, hydroxyl radicals $^{\bullet}OH$ and superoxide radicals $^{\bullet}O_2^-$) that rapidly mineralize UDMH and its toxic intermediates into harmless small molecules (CO_2 and H_2O), offering both high efficiency and broad applicability.[7] AOPs, including photocatalysis, Fenton/Fenton-like reaction, and low-temperature plasma treatment, have been extensively adopted to treat UDMH in water environments.[8–10] Although various AOPs have demonstrated remarkable efficiency in rapidly degrading UDMH, the mineralization rate remains unsatisfactory. For instance, the AgCo/SBA-15/PMS system achieved nearly 100% UDMH degradation within 15 min yet only attained a 20.8% mineralization rate after 30 min of reaction.[11] Notably, several transformation byproducts, such as

Department of Pharmaceutical & Biological Engineering, School of Chemical Engineering, Sichuan University, Chengdu 610065, China. E-mail: zhangyongkui@scu.edu.cn; Tel: +86-28-85405221

tetramethyl tetrazene (TMT), *N*-methyl-*N*-(methylideneamino) methanamine (FDNH), and nitrosodimethylamine (NDMA), show serious toxicity.[12] Therefore, the development of AOPs with powerful mineralization ability is extremely significant for the detoxification of UDMH.

Microwave-assisted catalytic oxidation processes have gained significant attention due to their ability to accelerate chemical reactions and the potential to completely degrade organic pollutants.[13] Microwave-assisted catalytic oxidation presents a reliable alternative to conventional oxidation methods for UDMH wastewater remediation, offering operational simplicity, rapid kinetics, and high degradation efficiency.[14] Therefore, microwave-assisted technology has gained widespread attention for applications in environmental catalysis.[15–18] Meanwhile, the non-thermal effects of microwaves (*e.g.*, high-frequency vibration of polar molecules) can enhance electron mobility at the active sites on the catalyst surface, promote redox cycling, and simultaneously reduce the accumulation of toxic intermediates.[19] Microwave-assisted catalytic technology effectively suppresses toxic intermediate formation during organic pollutant degradation by inducing rapid molecular excitation and thermal activation through dipole rotation, ultimately driving the intermediates towards CO_2 and H_2O.[20] For microwave reactions, the selection of microwave-absorbing materials is critical. Among numerous microwave-absorbing materials, manganese ores exhibit superior microwave absorption performance due to their broad absorption bands.[21] Extensive studies have demonstrated that microwave irradiation can effectively introduce or modulate oxygen vacancies in manganese oxide lattices, thereby substantially enhancing their catalytic functionality.[22,23] Concurrently, manganese oxide-based catalysis represents a versatile redox-active system integrating oxidative and catalytic capabilities, rendering it applicable to advanced oxidation processes for water treatment and air purification.[24,25] As representative manganese oxides, manganese dioxide (MnO_2) and manganese trioxide (Mn_2O_3) demonstrate significant catalytic potential in AOPs owing to their multivalent characteristics (Mn^{2+}/Mn^{3+}/Mn^{4+}) and tunable surface chemistry.[13,14,26,27] However, current research predominantly focuses on individual manganese oxides, lacking systematic investigation into how their electronic structure differences (*e.g.*, metallic *vs.* semiconductor properties) influence radical generation pathways and intermediate product distributions—a knowledge gap that hinders the rational design and application optimization of these catalysts. Furthermore, critical knowledge gaps remain in microwave-assisted manganese oxides catalytic degradation systems: (1) the regulatory mechanism of microwaves on the surface electronic structures of MnO_2 and Mn_2O_3 remains unclear; (2) the relationship between valence cycling pathways and intermediate product toxicity under microwave assistance requires urgent clarification.

To address these challenges, this study systematically investigates the catalytic performance and mechanistic distinctions between MnO_2 and Mn_2O_3 towards UDMH degradation under microwave assistance. By integrating first-principles calculations with comprehensive characterization, we elucidate how the structural and electronic properties of both oxides regulate catalysis. Furthermore, SPME-GC-MS analysis of intermediate distributions establishes the degradation pathway of UDMH catalyzed by MnO_2 and Mn_2O_3. This work provides theoretical foundations for the rational design of manganese-based catalysts and advances microwave-catalysis synergy for nitrogen-containing wastewater treatment.

2 Materials and methods

2.1 Materials and reagents

1,1-Dimethylhydrazine ($C_2H_8N_2$, >98%) was purchased from Shanghai Bidepharm Co., Ltd. Manganese trioxide (Mn_2O_3, >98%), manganese dioxide (MnO_2, >98%), formaldehyde 2,2-dimethyl hydrazone ($C_3H_8N_2$, >98%) and *N*-nitrosodimethylamine ($C_2H_6N_2O$, >99%) were purchased from Aladdin Co., Ltd. Other commonly used reagents of analytical grade were purchased from Chengdu Kelong Co., Ltd. The main parameters of the UDMH simulated wastewater used in this study are shown in Table S1 of the Supplementary Materials.

2.2 Degradation of UDMH

50 mL of UDMH wastewater was added to a 250 mL conical flask, followed by the addition of a specific dose of MnO_2 or Mn_2O_3 catalyst. The reaction system was then placed in a microwave reactor, connected to a circulating cooling-water condenser, and subjected to microwave irradiation at a set power for 30 min. After reaction, the catalyst was removed by filtration through a 0.22 μm membrane, and the residual UDMH concentration and chemical oxygen demand (COD) in the filtrate were measured using a UV-Vis spectrophotometer (AOE-A360). To further investigate the changes in formaldehyde and other nitrogen-containing intermediates during the degradation process, the degradation solution was analyzed by UV scanning (characteristic UV absorption wavelengths are listed in Table S3). The concentration of leached manganese ions during the reaction was determined with an inductively coupled plasma emission spectrometer (ICP-OES, Thermo Scientific iCAP 7400) (detailed test methods are provided in Text S1). Additionally, key reaction conditions, including the dosage of manganese oxides, the initial pH of the reaction solution, and the reaction time, were systematically optimized (detailed experimental conditions are listed in Table S2). At the same time, the toxicity of the intermediate product was analyzed using Ecological Structure Activity Relationships (Ecosar) software version 9.3. ECOSAR is a chemical compound ecotoxicity prediction system developed by the U.S Environmental Protection Agency.

2.3 Free radical quenching experiments

In an effort to detect the potentially generated active free radicals during the reaction process, a variety of free radical scavengers were employed in the reaction. L-Histidine and *tert*-butanol were utilized to scavenge $^1O_2$ and $^{\bullet}OH$, respectively, while $KBrO_3$ was employed to remove electrons in the reaction system.[28–30] Specifically, 50 mL of UDMH wastewater and

5 mmol L^{-1} of MnO_2 and Mn_2O_3 were added to a 250 mL conical flask. A scavenger with a concentration of 5 mmol L^{-1} (the molar ratio of [scavenger] to catalyst was 1 : 4) was introduced into each reaction group. The reaction was conducted in a microwave reactor for 5 min. Once the reaction was completed, the remaining UDMH content was determined in order to analyze the contribution of free radicals in the reaction system.

2.4 Characterization of catalyst and degradation intermediates

Crystal structures of the pristine and used catalysts were examined at room temperature using an X-ray diffractometer (Rigaku D/max-TTR III) with Cu Kα radiation (λ = 1.54056 Å), a current of 40 mA, and a voltage of 40 kV. X-ray photoelectron spectroscopy (XPS) analysis of the elemental states on the catalyst surface was conducted with a Thermo Scientific ESCALAB 250Xi spectrometer (Kratos Axis Ultra DLD, Al-Kα, X-ray source). The composition of the reaction solution was determined *via* solid-phase microextraction gas chromatography-mass spectrometry (SPME-GC-MS, QP2010 Ultra); the detailed detection conditions are shown in Text S2.

2.5 DFT calculations

All geometry optimisations and electronic-structure calculations were performed with periodic boundary conditions using density-functional theory (DFT) as implemented in CASTEP (Materials Studio 2020). The generalised-gradient approximation (GGA) in conjunction with the Perdew–Burke–Ernzerhof (PBE) functional was employed to describe the exchange–correlation. Ultrasoft pseudopotentials were used for the ion–valence interaction, and the Kohn–Sham orbitals were expanded in plane waves with a cut-off energy of 500 eV after convergence tests. The convergence thresholds for geometry optimisation were set to: energy $\leq 5 \times 10^{-6}$ eV per atom, maximum pressure $\leq$ 0.1 GPa, maximum force $\leq$ 0.05 eV $Å^{-1}$, and maximum displacement $\leq 2 \times 10^{-3}$ Å. DFT-D corrections with the Tkatchenko–Scheffler (TS) scheme were applied to account for van der Waals and dispersion interactions. Owing to the strongly localised Mn-3d electrons, GGA + U was adopted with U = 3.81 eV to reduce self-interaction error. Spin polarisation was included for all Mn atoms. Brillouin-zone integration was carried out using the Monkhorst–Pack grid with a 1 × 1 × 1 k-point mesh.

After relaxation, the lattice parameters of the MnO_2 unit cell were $a = b$ = 2.9404 Å, c = 4.6555 Å, in good agreement with the experimental values ($a = b$ = 4.4041 Å, c = 2.8765 Å). The (102) surface is the thermodynamically most stable facet of MnO_2 and exhibits high catalytic activity. A 10 Å vacuum slab was inserted along the surface normal to eliminate spurious interactions between periodic images. For Mn_2O_3, the optimised cell parameter is $a = b = c$ = 8.1484 Å, consistent with the experimental data ($a = b$ = 4.4041 Å, c = 2.8765 Å). The (222) termination was chosen because it is the most stable exposed surface of Mn_2O_3 and possesses excellent catalytic properties; a 10 Å vacuum region was also applied.

The oxygen-vacancy formation energy was calculated according to:

$$E_{vac} = E_{defect} - E_{perfect} + \mu_O$$

where E_{defect} and $E_{perfect}$ are the total energy of the slab containing the vacancy and the pristine slab, respectively, and μ_O is the oxygen chemical potential referenced to $\frac{1}{2}O_2$.

The adsorption energy of UDMH on the catalyst surface was evaluated as:

$$E_{ads} = E_{slab+UDMH} - E_{slab} - E_{UDMH}$$

where $E_{slab+UDMH}$ is the total energy of the adsorbed system, E_{slab} is the clean surface energy, and E_{UDMH} is the energy of an isolated UDMH molecule; a negative E_{ads} indicates an exothermic adsorption process.

3 Results and discussion

3.1 Catalytic performance and stability

MnO_2 and Mn_2O_3 exhibited distinct catalytic performance in the microwave-assisted UDMH degradation process. Under

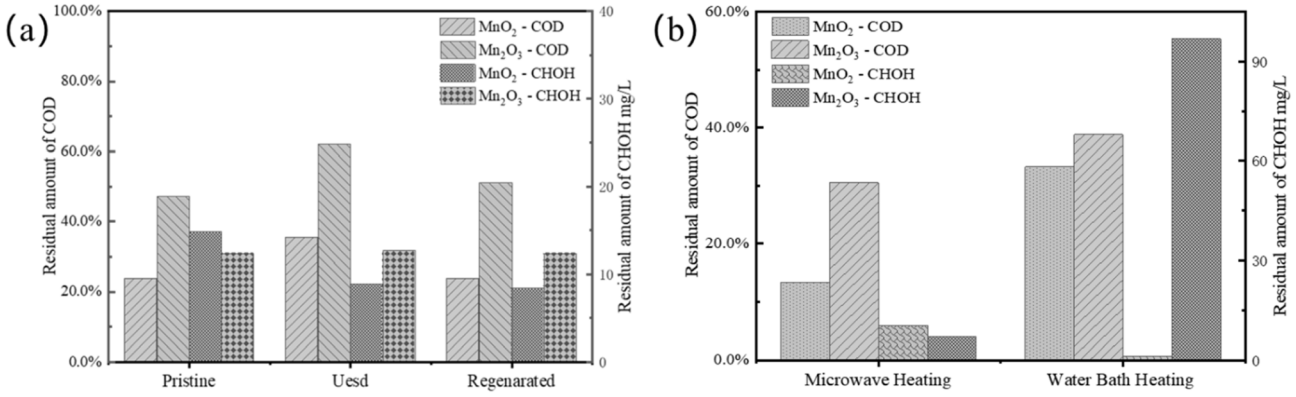

Fig. 1 Comparative catalytic performance and stability of MnO_2 and Mn_2O_3 in UDMH degradation: (a) under microwave-assisted conditions, showing COD removal efficiency, formaldehyde degradation efficiency, and recyclability tests *via* thermal regeneration; (b) under microwave-assisted and water-bath heating conditions, showing COD removal efficiency and formaldehyde degradation efficiency.

identical conditions, microwave irradiation consistently outperformed conventional water-bath heating in terms of both COD removal efficiency and residual formaldehyde concentration (Fig. 1b). These results demonstrate that microwave assistance effectively enhances the catalytic activity. Specifically, the MnO_2 system demonstrated superior COD

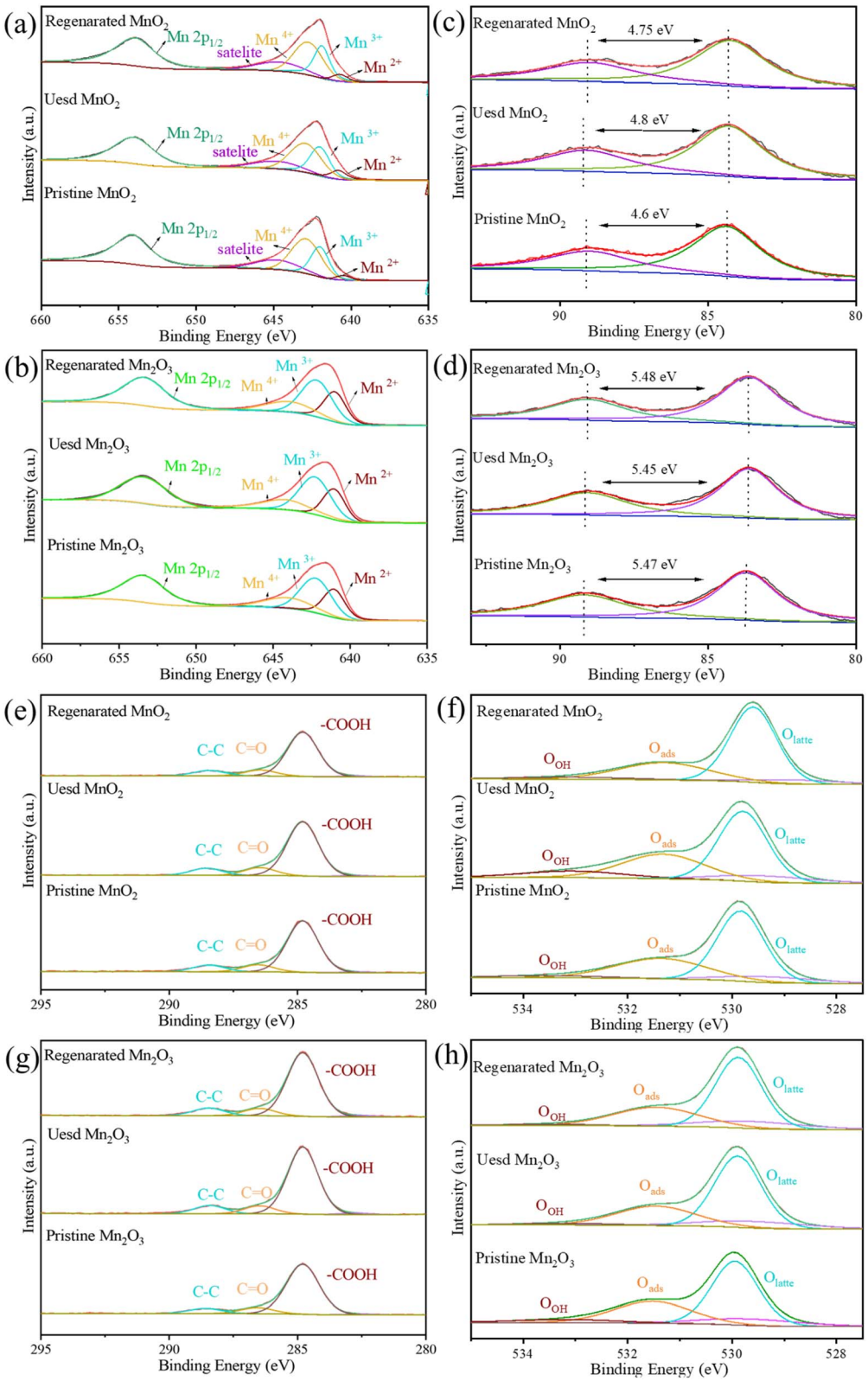

Fig. 2 Comparative XPS analysis of MnO_2 and Mn_2O_3: (a) Mn 2p of MnO_2, (b) Mn 3s of MnO_2, (c) Mn 2p of Mn_2O_3, (d) Mn 3s of Mn_2O_3, (e) C 1s of MnO_2, (f) O 1s of MnO_2, (g) C 1s of Mn_2O_3, and (h) O 1s of Mn_2O_3.

Table 1 Relative content of MnO_2/Mn_2O_3: pristine, used, and regenerated states

		Percentage (%)					
		MnO_2			Mn_2O_3		
Elements	Assignment	Pristine	Used	Regenerated	Pristine	Used	Regenerated
Mn	Mn^{4+}	60.6	52.4	55.4	23.41	25.16	21.54
	Mn^{3+}	35.4	36.9	38.1	46.61	47.89	48.53
	Mn^{2+}	4.0	10.7	6.5	29.98	26.95	29.93
C	–COOH	10.2	10.4	9.7	8.4	9.7	9.7
	C=O	10.9	11.5	10.8	9.8	9.9	9.5
	C–C	78.9	78.1	79.5	81.8	80.4	80.8
O	OOH	5.4	10.9	4.8	6.6	3.3	2.6
	O_{ads}	30.8	33.4	29.4	33.9	30.6	32.3
	O_{latt}	63.8	55.7	65.8	59.5	65.9	65.1

removal efficiency (Fig. 1a). However, the Mn_2O_3 system demonstrated accelerated degradation kinetics toward formaldehyde. This difference in oxidation selectivity suggests the existence of distinct UDMH reaction pathways in the microwave-assisted MnO_2 and Mn_2O_3 degradation systems, which might be determined by the different electronic structures and surface chemistry between MnO_2 and Mn_2O_3. Recyclability tests were further conducted to evaluate the stability differences of the two manganese oxides (Fig. 1). Both MnO_2 and Mn_2O_3 showed reduced activity after the first cycle, with Mn_2O_3 experiencing more significant deactivation. Thermal regeneration at 450 °C for 4 h in a muffle furnace effectively restored the catalytic activity of both MnO_2 and Mn_2O_3, with COD removal efficiency recovering to levels comparable to their initial performance. Notably, MnO_2 exhibited lower residual formaldehyde, indicating superior COD removal activity and cyclic stability compared to Mn_2O_3.

To elucidate the mechanism underlying the catalytic performance differences between MnO_2 and Mn_2O_3, systematic characterizations were conducted to analyze critical differences in the crystalline stability, surface valence states, and functional group evolution between MnO_2 and Mn_2O_3 during the reaction process. XRD analysis (Fig. S1) verified the structural stability of MnO_2 (PDF# 97-007-6430) and Mn_2O_3 (PDF# 04-007-0856) during degradation and regeneration and indicated the exposed crystal plane of MnO_2 (102) and Mn_2O_3 (222). Although Mn_2O_3 exhibited a higher Mn^{2+} leaching concentration (119 mg L^{-1} with a leaching rate of 0.27%) compared to MnO_2 (3.5 mg L^{-1} with a leaching rate of 0.02%), neither catalyst displayed lattice distortion or structural collapse. To further verify the structural robustness, Mn_2O_3 was subjected to comprehensive post-cycling characterization following five consecutive catalytic runs. XRD and XPS analyses confirmed the preservation of the crystalline phase and the oxidation state integrity, with neither detectable phase transformation nor appreciable variation in manganese speciation observed (Fig. S1). These findings are consistent with the sustained catalytic performance demonstrated across multiple cycles.

The results of XPS analysis (Fig. 2 and Table 1) comprehensively revealed the valence-state evolution processes and the differences in the surface chemical behavior of MnO_2 and Mn_2O_3 during the microwave-assisted degradation of UDMH. Deconvolution of the Mn 2p peaks indicated that the content of Mn^{2+} and Mn^{3+} in MnO_2 increased significantly after the reaction, showing a transformation from Mn^{4+} to Mn^{2+} and Mn^{3+}. For Mn_2O_3, the proportion of Mn^{4+} increased after the reaction, indicating that a conversion from Mn^{2+} and Mn^{3+} to Mn^{4+} occurred.[31–35] This was further confirmed by analysis of the Mn 3s peak. The average oxidation state (AOS) of Mn could be calculated using the energy separation (ΔE_{mn3s}) of the Mn 3s doublet, following the formula: AOS = 8.95–1.13ΔE_{mn3s} (eV).[36] For pristine, used, and regenerated MnO_2 samples, the spin-energy separations of the Mn 3s peaks were determined to be 4.6, 4.8, and 4.75 eV, respectively, corresponding to average Mn oxidation states of +3.75, +3.53, and +3.58. In contrast, for pristine, used, and regenerated Mn_2O_3 samples, the Mn 3s spin-energy separations were 5.47, 5.45, and 5.48 eV, respectively, yielding average Mn oxidation states of +2.77, +2.79, and +2.76, respectively. This phenomenon fully demonstrated the existence of a Mn^{2+}/Mn^{3+}/Mn^{4+} valence-state cycle in both systems. In the microwave-catalyzed system, however, additional electron transfer induced by microwaves promotes manganese ion leaching. Notably, Mn_2O_3 exhibits higher leaching than MnO_2. Combined with the results of recyclability tests, it could be elucidated that the stable high valence state of MnO_2 and the dynamic Mn^{3+}/Mn^{4+} cycle work synergistically, significantly enhancing the generation efficiency of reactive oxygen species; however, the Mn^{2+} dissolution in Mn_2O_3 might inhibit the further progress of the reaction, and its long-term stability was limited by the loss of active components.[37] The above findings indicate a redox-mediated catalytic process by manganese oxides during the microwave-assisted degradation of UDMH, and the increased electron transport rate is the reason for the enhanced catalytic ability.

Further analysis of oxygen species shows that, after the reaction, the proportion of hydroxyl oxygen (O–OH) on the surface of the MnO_2 increases, while the content of O–OH on the surface of Mn_2O_3 decreases.[32] Combined with the fact that MnO_2 exhibits a higher COD removal efficiency for UDMH than Mn_2O_3, it can be inferred that MnO_2 is more effective in dissociating surface water

molecules to generate ˙OH, which indirectly confirms its stronger capability to produce surface-bound ˙OH.

In addition, analysis of the C 1s spectrum indicates that, after the reaction, more C=O and –COOH groups are present on the surface of the Mn_2O_3.[38] This phenomenon suggests that the surface of Mn_2O_3 is more likely to adsorb oxygen-containing intermediates, and this adsorption may hinder the active sites, thereby leading to the deactivation of the catalyst.[39]

In conclusion, the high catalytic activity of MnO_2 is attributed to its dynamic $Mn^{2+}/Mn^{3+}/Mn^{4+}$ cycle, strong ˙OH generation ability, and surface self-cleaning characteristics. For Mn_2O_3, due to the relatively low stability of Mn^{3+} and its susceptibility to poisoning by the intermediates, its catalytic performance is limited to a certain extent.

3.2 Effects of typical reaction parameters on UDMH degradation

3.2.1 Dosage of the catalyst. The influence of catalyst dosage on the UDMH degradation pathway and intermediate distribution is illustrated in Fig. 3. At low concentrations ($\leq$40 mmol L^{-1}), the Mn_2O_3 system generates significantly more intermediates (*e.g.*, TMT, FDMH, and NDMA) than the MnO_2 system. This behavior is attributed to the accumulation of intermediates due to the low oxidation capacity of Mn_2O_3 at low concentrations. In contrast, at high concentrations ($\geq$100 mmol L^{-1}), the MnO_2 system favors TMT formation, driven by its high surface $Mn^{2+}/Mn^{3+}/Mn^{4+}$ cycle density that increases the formation of ˙OH and enhances oxidation capacity, facilitating the conversion of NDMA/FDMH into TMT. For Mn_2O_3, the reduction of complex products, such as TMT, might be due to the higher Mn^{3+}/Mn^{2+} content, with Mn^{2+} having a stronger electron donor ability than Mn^{4+}, leading to the reduction of TMT.[40]

As shown in Fig. 3c–e, increasing the catalyst dosage could reduce COD in both systems, with MnO_2 demonstrating superior performance due to its stable Mn^{4+} dominance and the production of more free radicals, enabling efficient mineralization of organics to CO_2/H_2O. The divergent trends in residual formaldehyde reflect the catalytic capacity: for MnO_2,

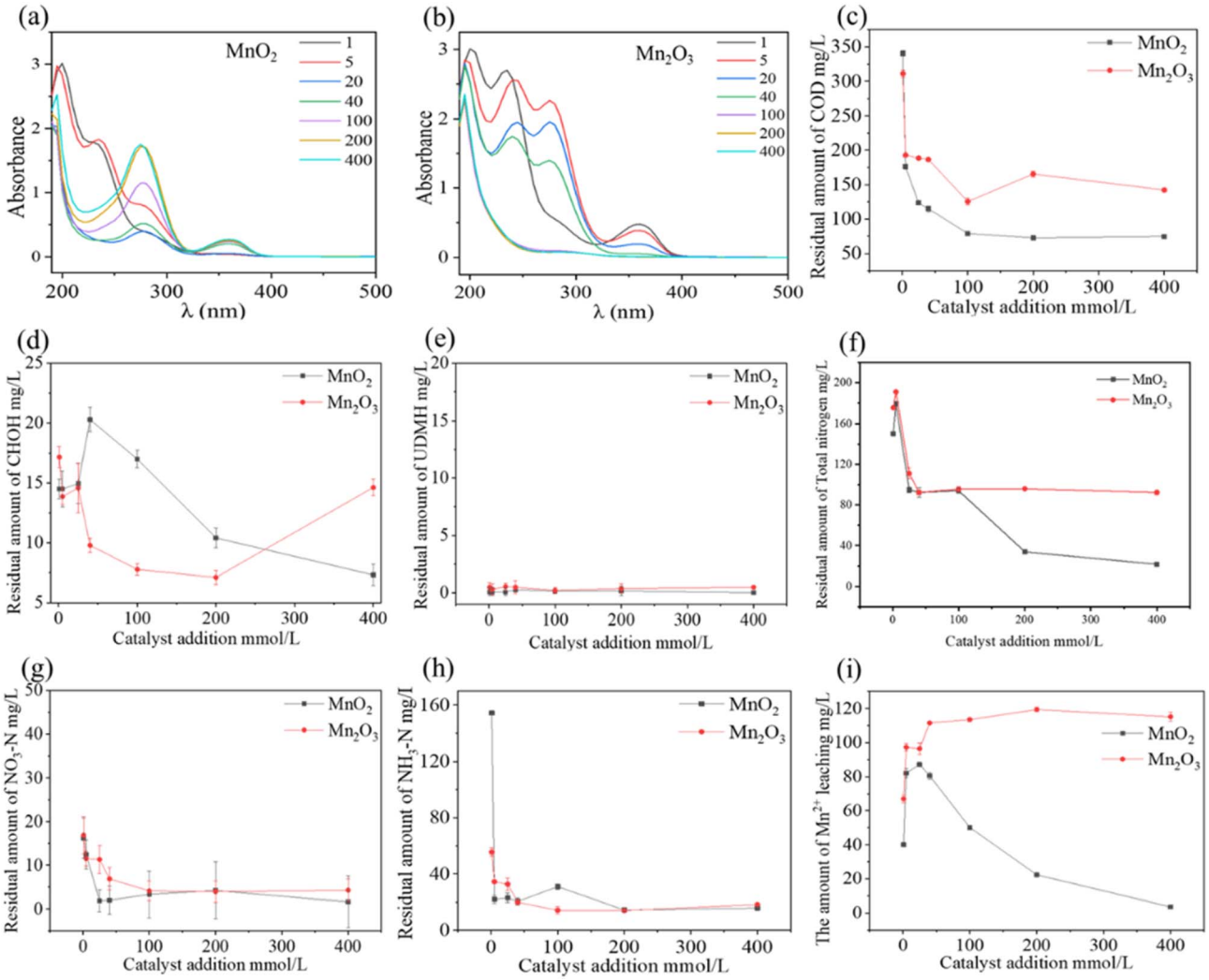

Fig. 3 Effect of MnO_2/Mn_2O_3 loading on UDMH degradation efficiency. (a and b) Full UV wavelength spectra, and the amount of (c) COD, (d) CHOH, (e) UDMH, (f) total nitrogen, (g) NO_3–N, (h) NH_3–N, and (i) Mn^{2+} after the reaction.

formaldehyde first accumulates and then decreases. The generated free radicals preferentially convert UDMH and some intermediates into simple products, such as formaldehyde, at low doses, while formaldehyde would be mineralized by more free radicals at high doses. In contrast, for Mn_2O_3, Mn^{2+}-mediated free radicals at low dosages produce more intermediate products without further mineralization, while at high dosages, additional radicals degrade these intermediates into formaldehyde. Notably, both catalysts achieve excellent UDMH degradation (residual <5%), indicating comparable abilities to cleave the initial C–N bond, but differ in intermediate conversion.

The nitrogen migration analysis (Fig. 3f–h) reveals that MnO_2 outperforms Mn_2O_3 in total nitrogen removal, especially at high doses, which is attributed to its strong oxidizing Mn^{2+}/Mn^{3+}/Mn^{4+} cycle, which efficiently converts organic nitrogen into N_2 or surface-bound species, while suppressing NDMA formation. In contrast, the lower oxidation capacity of Mn_2O_3 may lead to incomplete removal. The enhanced hydroxyl oxygen on MnO_2 further aids nitrogen intermediate adsorption-oxidation, supporting its superiority in nitrogen-containing wastewater treatment.[41]

Manganese ion leaching experiments (Fig. 3i) highlight structural differences: Mn_2O_3 shows steady Mn^{2+} leaching (stabilizing at 111 mg L^{-1} at 40 mmol L^{-1}), prompting systematic evaluation of homogeneous catalysis *via* dissolved manganese species. As summarized in Table S6, supplementation with a certain amount of Mn^{2+} concentrations marginally enhanced the catalytic performance, establishing that homogeneous contributions remain secondary. In contrast, MnO_2 exhibits a leaching trend of initial increase followed by a sharp decrease (<5 mg L^{-1}), attributed to its surface hydroxyl oxygen adsorbing Mn^{2+} to form a passivation layer, coupled with stable Mn^{4+} valence states that minimize active component loss.[42] These results emphasize the superior structural stability of MnO_2, which is critical for long-term catalytic applications. Collectively, both oxides operate predominantly as heterogeneous catalysts; the minor homogeneous component associated with Mn_2O_3 merely exerts a modest facilitative effect without altering the fundamental surface-mediated mechanism.

3.2.2 Initial pH of the solution. As shown in Fig. 4, the initial pH deeply influences the catalytic pathways of MnO_2 and Mn_2O_3. Both catalysts exhibit the best comprehensive degradation performance under neutral conditions (pH 7) (Fig. 4a–h),

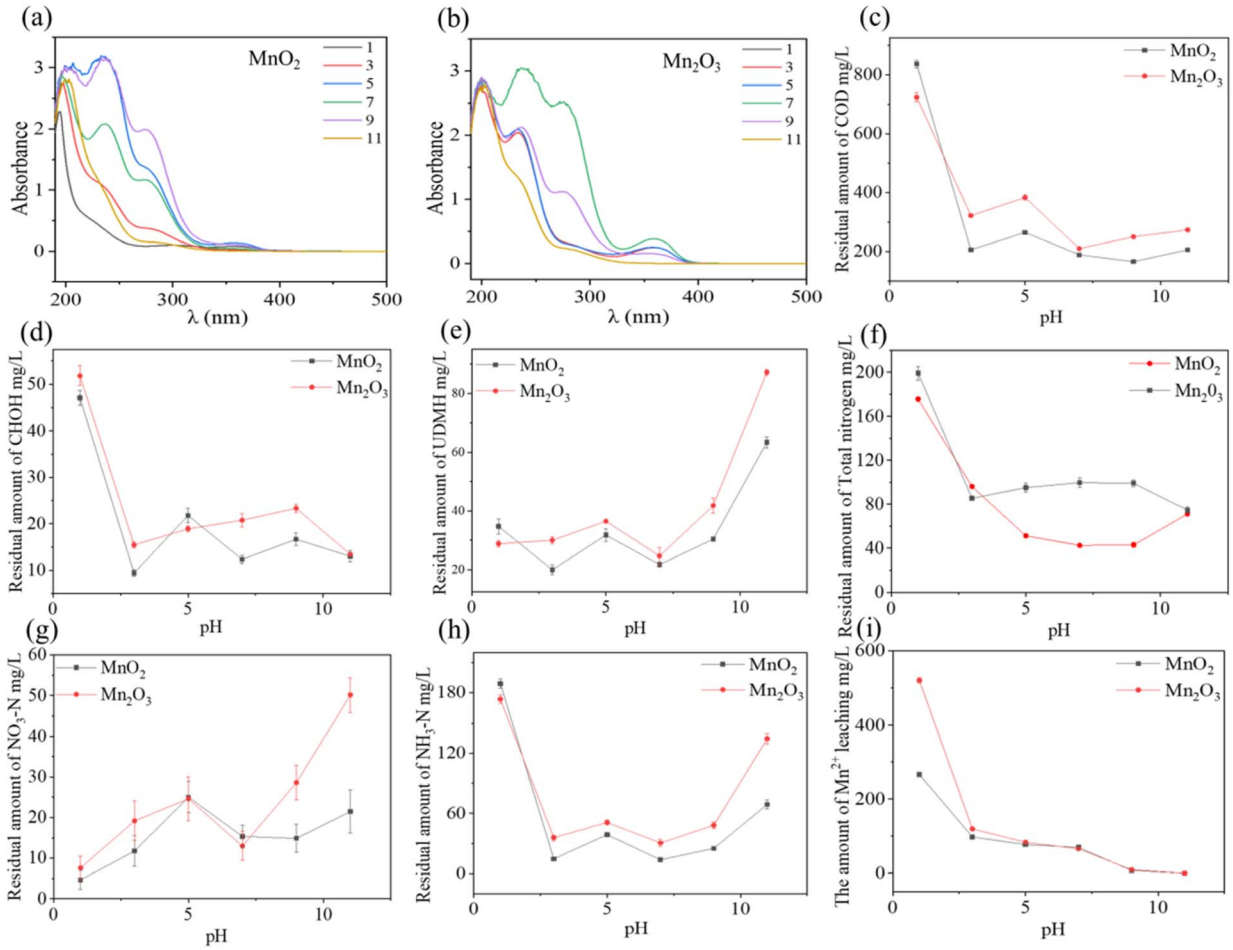

Fig. 4 Effect of different initial pH values on UDMH degradation efficiency. (a and b) Full UV wavelength spectra, and the amount of (c) COD, (d) CHOH, (e) UDMH, (f) total nitrogen, (g) NO_3–N, (h) NH_3–N, and (i) Mn^{2+} after the reaction.

although MnO_2 demonstrates overall superior degradation efficiency compared to Mn_2O_3. This is attributed to the enhanced degree of surface hydroxylation of the catalysts in the neutral environment, which promotes the generation of ˙OH and deep oxidation of organic compounds. Under extreme acidic (pH 1) or alkaline (pH 11) conditions, the MnO_2 system generates fewer intermediates, likely due to pH-induced structural alterations that inhibit catalytic activity—for example, partial conversion of δ-MnO_2 to hausmannite at pH 4 disrupts the surface redox cycle.[43] In contrast, Mn_2O_3 exhibits the fewest intermediate products under non-neutral pH conditions but accumulates intermediates at pH 7. The acidic medium protonated the Mn_2O_3 surface, imparting a net positive charge that weakened electrostatic attraction to the negatively charged reaction substrate.[44] At the same time, the degradation effect would be reduced slightly when the alkalinity is higher. This is because excess OH- inhibits the production of ˙OH.[45] The lowest residual nitrate nitrogen at pH 1 may be due to the acidic conditions disfavoring nitrification reactions (*e.g.*, $NH_3 \rightarrow NO_3^-$), while the high oxidizing property of MnO_2 could further reduce nitrate nitrogen to N_2, resulting in significantly better nitrogen removal efficiency than Mn_2O_3 (Fig. 4f–h). Meanwhile, the high oxidizing capacity of MnO_2 also contributes to its superior comprehensive degradation performance over Mn_2O_3.

Manganese ion leaching (Fig. 4i) reveals distinct pH-dependent stability: under alkaline conditions (pH ≥ 9), Mn^{2+} leaching approaches zero for both catalysts, as OH^- precipitates $Mn(OH)_2$, which forms a MnO_2-like passivation layer *via* microwave-induced dehydration (XRD confirms no new phases, indicating structural consistency).[46] In contrast, acidic conditions (pH ≤ 3) exacerbate Mn_2O_3 dissolution (Mn^{2+} leaching two times higher than for MnO_2), aligning with its Mn^{3+} disproportionation-driven homogeneous catalysis. The low leaching of MnO_2 over a wide pH range (especially in alkaline environments) ensures the long-term structural integrity of MnO_2, which is a key advantage for practical applications.

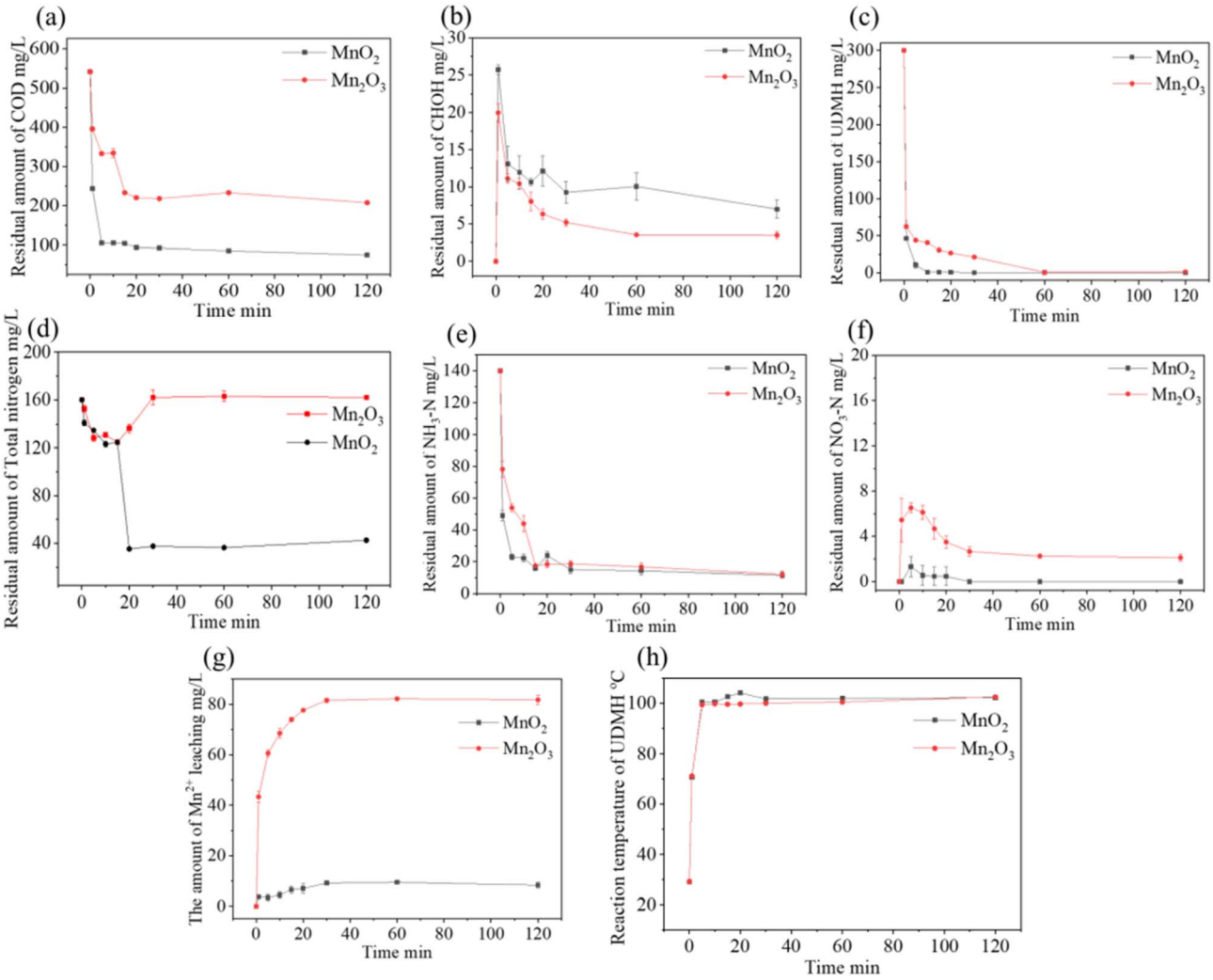

Fig. 5 Dynamic curves of UDMH degradation in the microwave-assisted manganese oxide catalytic oxidation process: Comparative analysis of MnO_2 and Mn_2O_3: (a) COD residual concentration, (b) formaldehyde residual concentration, (c) UDMH residual concentration, (d) total nitrogen residual concentration, (e) ammonia nitrogen residual concentration, (f) nitrate nitrogen residual concentration, (g) manganese ion leaching concentration, and (h) reaction temperature.

Table 2 Comparison of selected recent literature studies on UDMH degradation

No.	Method of degradation	UDMH (mg L^{-1})	Reaction volume (mL)	Removal efficiency	k (min^{-1})	References
1	Photocatalysis/TiO_2/SBA-15	100	230	60 min 80%	0.02511	8
2	Catalytic activation of PMS/SBA-15 supported Co-based bimetallic catalysts	100	200	15 min 100%	0.1177	48
3	UVC/H_2O_2	100	250	20 min 100%	0.2050	49
4	UVC/PMS	100	250	30 min 100%	0.1724	49
5	Photocatalytic/Ag/β-cyclodextrin co-doped TiO_2	20	20	80 min 96.8%	0.037	50
6	Catalytic wet peroxide oxidation/ chitosan–silica nanoparticles catalyst	500	50	10 min 100%	—	51
7	Low temperature plasma generated	—	—	10 min 95%	1.6825	52
8	Biodeterioration	—	—	126 d 88%	—	53
9	Microwave catalysis/Mn_2O_3/MnO_2	300	50	60 min 99.8%	—	This study

Initial pH critically governs the catalytic pathways of MnO_2 and Mn_2O_3. Both achieve optimal degradation at pH 7, with MnO_2 consistently outperforming Mn_2O_3. Neutral media intensify surface hydroxylation, boosting $^{\bullet}OH$ production, whereas extreme acidity/alkalinity deactivate the catalysts *via* structural transformation or inhibition of $^{\bullet}OH$. Under acidic conditions, Mn_2O_3 leaches markedly more Mn^{2+} than MnO_2, while both exhibit negligible dissolution at pH $\geq$ 9 owing to surface passivation, indicating the long-term structural robustness of MnO_2.

3.2.3 Experimental study on kinetics. Kinetic experiments revealed the time-dependent evolution of key components during UDMH degradation (Fig. 5a–h). Residual COD, formaldehyde, and UDMH exhibited monotonically decreasing trends, stabilizing after 60 min, indicating pseudo-first-order kinetics and reaction completeness. In contrast, nitrate nitrogen displayed a unique trend of initial increase followed by decrease, attributed to two sequential processes: early-stage oxidation of nitrogen-containing intermediates (*e.g.*, NDMA) to NO_3^-, and subsequent reduction to N_2 or surface-bound nitrogen species driven by surface active sites on the catalysts.[47] Meanwhile, compared with similar catalytic studies (Table 2), this research demonstrates unique advantages in the catalytic degradation of UDMH. Specifically, the degradation efficiency of UDMH reaches over 99% within 60 minutes, which is superior to that of comparable catalytic systems.

The Mn^{2+} concentration initially increased due to the dynamic dissolution of the catalyst, but reached an adsorption–oxidation equilibrium in the later stage. Notably, the amount of Mn^{2+} leached from MnO_2 was much lower than that from Mn_2O_3, which could be attributed to the complexation of Mn^{2+} by the surface hydroxyl oxygen groups on MnO_2. This equilibrium suppressed further leaching, aligning with the stable residual Mn^{2+} concentration after 60 min (Fig. 5g). The reaction temperature reached its peak within 5 minutes, with the average reaction temperature of MnO_2 being slightly higher than that of Mn_2O_3, which may correspond to its more thorough mineralization. The final mineralization results are presented in Table 3, where the total organic carbon (TOC) content of both samples decreased by approximately half, demonstrating their excellent oxidative capacity. The convergence of all indicators at 60 min confirmed the synergistic interplay between free-radical chain reactions and surface catalytic cycles, validating this duration as optimal for thorough degradation while minimizing secondary pollution risks.

3.3 Investigation of the reaction mechanism

Free-radical quenching experiments (Fig. 6) reveal that microwave-assisted degradation of UDMH by manganese oxides involves the synergistic action of $^{\bullet}OH$, $^1O_2$, and e^-, with $^{\bullet}OH$ identified as the dominant species. The significant drop in degradation efficiency upon adding *tert*-butanol (TBA, $^{\bullet}OH$ quencher), far exceeding the inhibitory effects of L-histidine ($^1O_2$ quencher) and $KBrO_3$ (e^- quencher), confirms that $^{\bullet}OH$ is the key reactive oxygen species. This result aligns with the increased number of surface hydroxyl oxygen species (O–OH) on MnO_2 observed in the XPS analysis.

In the Mn_2O_3 system, the addition of *tert*-butanol (TBA, a $^{\bullet}OH$ scavenger) resulted in a much stronger inhibition of UDMH degradation compared to the MnO_2 system. This

Table 3 Mineralization of UDMH using the microwave-assisted manganese oxide catalytic oxidation process: comparative analysis of MnO_2 and Mn_2O_3

	TOC (mg L^{-1})	COD (mg L^{-1})
Reaction solution	81.76	543.05
MnO_2	40.94	93.64
Mn_2O_3	45.41	220.27

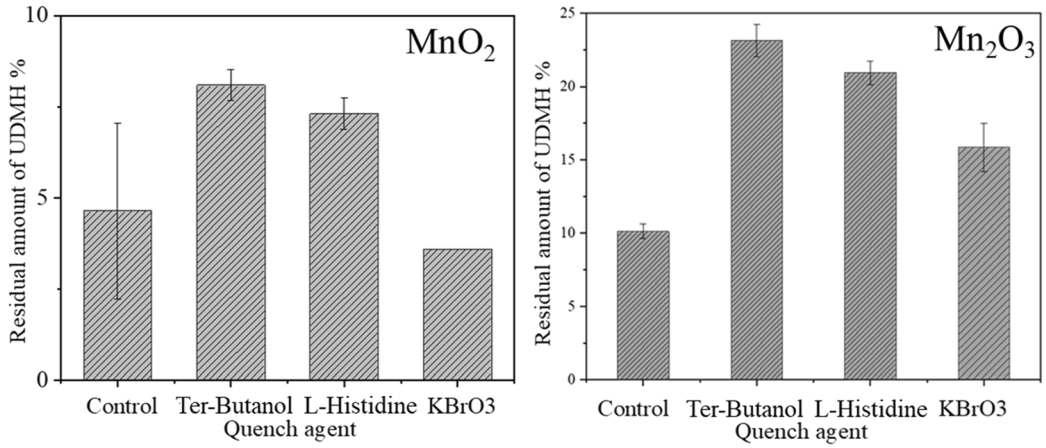

Fig. 6 Results of free radical quenching experiments.

observation indicates that the contribution of bulk hydroxyl radicals in the Mn_2O_3 system is higher than that in the MnO_2 system, which is consistent with the previously discussed disproportionation-driven homogeneous catalysis mechanism. In summary, MnO_2 enables efficient generation of $^{\bullet}OH$ through the surface $Mn^{4+}/Mn^{3+}/Mn^{2+}$ redox cycle, dominating the heterogeneous catalytic process. In contrast, Mn_2O_3 exhibits a unique dual functionality: in addition to the heterogeneous pathway, it generates $^{\bullet}OH$ *via* surface Mn^{3+} disproportionation, thereby achieving a homogeneous-heterogeneous synergistic catalytic route. These fundamental differences in catalytic mechanisms explain their distinct degradation efficiencies and intermediate product distributions.

To elucidate structure–activity relationships, the physicochemical properties of MnO_2 and Mn_2O_3 were systematically characterized. As shown in Fig. S4, both oxides exhibit type IV

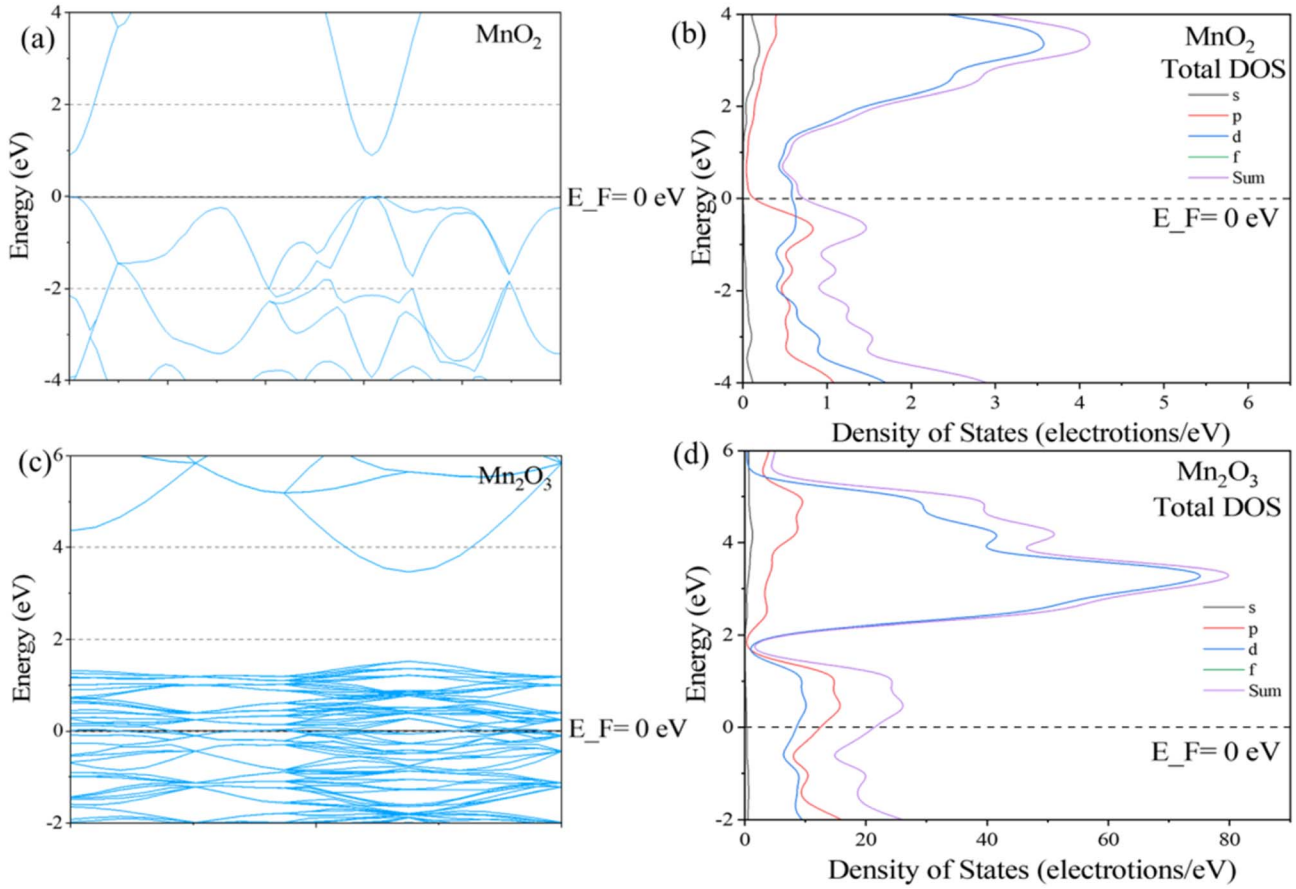

Fig. 7 Analysis of energy bands and density of states (DOS) of MnO_2 and Mn_2O_3: (a) band structure of MnO_2, (b) DOS of MnO_2, (c) band structure of Mn_2O_3, and (d) DOS of Mn_2O_3.

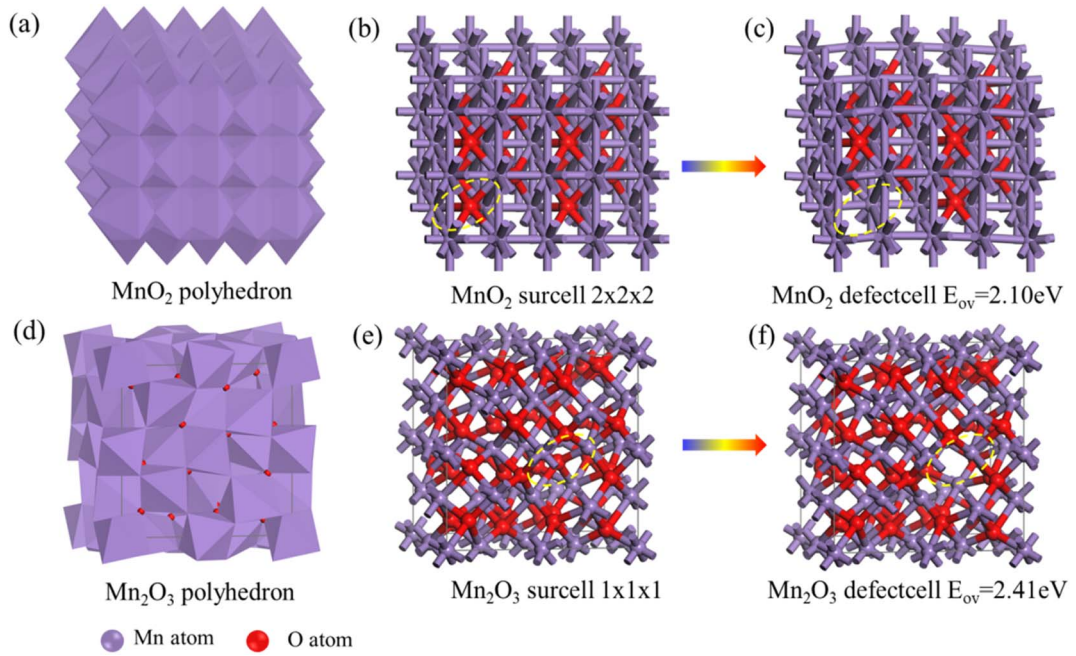

Fig. 8 Formation energy of oxygen vacancies over different manganese oxides: (a) polyhedron of MnO_2, (b) supercell of MnO_2, (c) defectcell of MnO_2, (d) polyhedron of Mn_2O_3, (e) supercell of Mn_2O_3, and (f) defectcell of Mn_2O_3.

isotherms with H3 hysteresis loops, characteristic of mesoporous architectures assembled from aggregated plate-like particles. Notably, Mn_2O_3 displays a substantially larger hysteresis loop area than MnO_2, indicating a more developed mesoporous network despite its lower specific surface area. This apparent contradiction arises from the significantly larger average pore diameter of Mn_2O_3 (22.07 nm) compared to MnO_2 (8.57 nm), as broader pores generate more pronounced capillary condensation and evaporation hysteresis (Table S5). Consistent with this interpretation, MnO_2 possesses a fourfold higher Brunauer–Emmett–Teller (BET) specific surface area (44.89 m^2 g^{-1}) relative to Mn_2O_3 (10.51 m^2 g^{-1}), alongside enhanced micropore area (3.46 *versus* 2.03 m^2 g^{-1}) and micropore volume (0.00189 *versus* 0.00092 cm^3 g^{-1}). These parameters corroborate its hierarchically porous structure with greater surface curvature and micropore-mediated active-site density. Particle size distributions centered at 1.70 μm (MnO_2) and 3.48 μm (Mn_2O_3) indicate comparable colloidal dimensions that preclude transport limitations as the origin of activity divergence (Fig. S4c and f). The divergent textural advantages—MnO_2 with superior specific surface area and microporosity, Mn_2O_3 with greater total pore volume—demonstrate that neither physical parameter alone governs catalytic performance. Instead, electronic properties and Mn(IV)-mediated redox dynamics constitute the dominant mechanistic drivers under microwave-assisted conditions.

Based on the structural models from XRD data, DFT calculations reveal pronounced differences in the energetic and electronic properties of MnO_2 and Mn_2O_3. Normalized total-energy computations confirm that MnO_2 possesses lower energy (−1650.77 eV *vs.* −1408.86 eV for Mn_2O_3), implying superior structural stability, which underpins its enhanced resistance to manganese leaching. Combined band-structure and density-of-states analyses (Fig. 7) further show that the valence-band maximum and conduction-band minimum of MnO_2 coincide at the same *k*-point, giving a direct band gap with vanishing density of states at the Fermi level (EF); this intrinsic semiconducting behavior implies only weak electron-transport effects on surface reactivity. In contrast, Mn_2O_3 exhibits bands crossing EF and a finite DOS at EF, manifesting metallic conductivity; consequently, electron transfer is highly efficient and strongly modulates surface chemistry, consistent with the more pronounced radical quenching observed in our earlier experiments.

To quantitatively compare oxidation and oxygen-release capabilities, we calculated the surface oxygen-vacancy (V_o) formation energies. MnO_2 exhibits a V_o value of 2.10 eV, whereas Mn_2O_3 reaches 2.41 eV, consistent with previous reports.[54] Density-functional results reveal that MnO_2 (2.10 eV) forms surface V_o more readily than Mn_2O_3 (2.41 eV) (Fig. 8). This disparity is rooted in their electronic structures: the narrow band gap of MnO_2 positions the Mn-3d states across the Fermi level, enabling facile electron localization–delocalization transitions at a low energy cost and thereby markedly lowering the V_o formation barrier. In contrast, the wide band gap of Mn_2O_3 pushes Mn-3d states toward the conduction-band minimum, demanding greater thermal activation for defect creation. Under the oxygen-lean conditions typical of catalytic reactions, MnO_2 will therefore sustain a higher V_o concentration than Mn_2O_3, supplying more vacancy-mediated *OH → *O → *OOH sites for sequential oxygen exchange and endowing MnO_2 with superior intrinsic OER activity and a lower overpotential.

Optimised MnO_2 and Mn_2O_3 slabs were obtained by cleaving five-layer (102) and (222) terminations, respectively, and

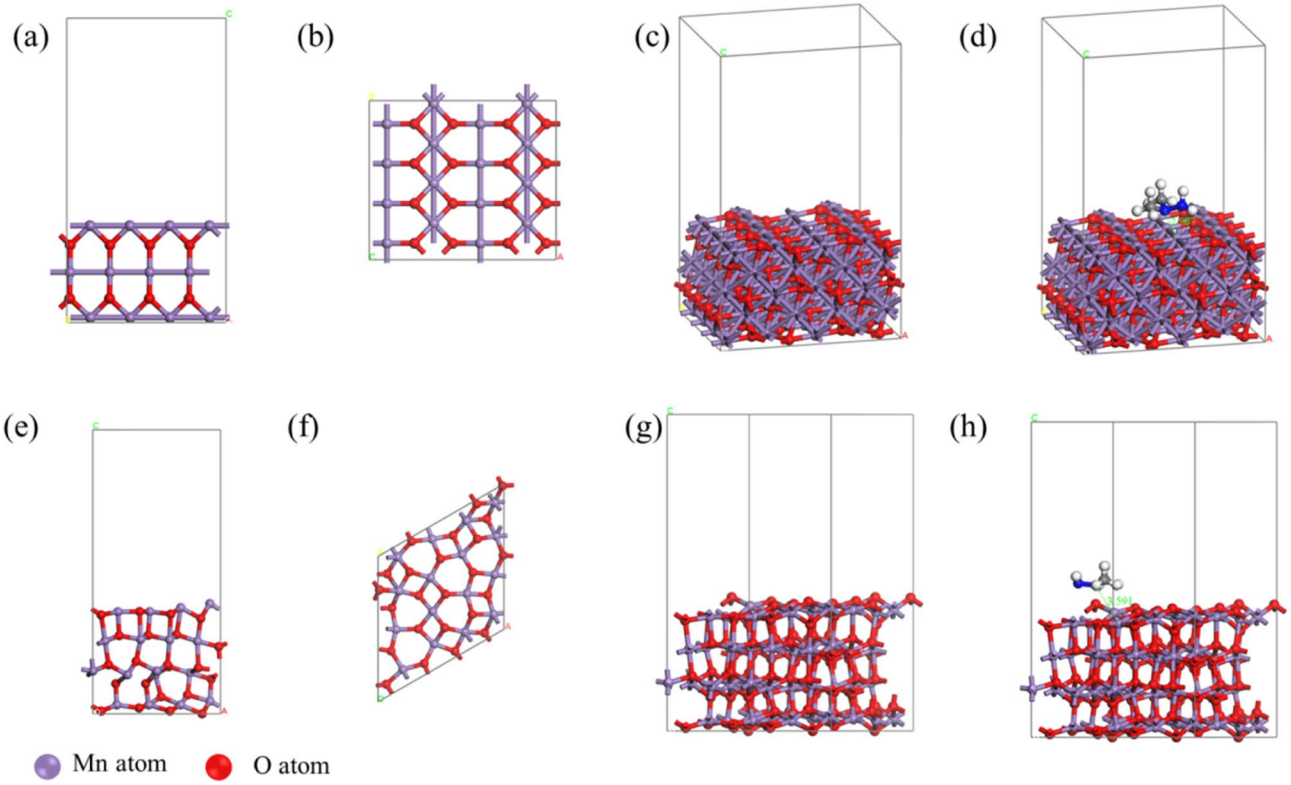

Fig. 9 Configuration of UDMH adsorption on the MnO_2 (102) and Mn_2O_3 (2220) surfaces. (O atoms are red; N atoms are blue; Mn atoms are purple; and cyan dashed lines indicate the distance between UDMH molecules and the supercell surface in Å): (a and b) side and top views of the MnO_2 (102) surface; (c and d) MnO_2 supercell before and after UDMH adsorption; (e and f) side and top views of the Mn_2O_3 (2220) surface; (g and h) Mn_2O_3 supercell before and after UDMH adsorption.

expanding them into 2 × 2 × 2 and 1 × 1 × 1 supercells with a 10 Å vacuum gap. After relaxation, the nitrogen atom closer to the UDMH backbone exhibited the highest nucleophilicity and electrophilicity; consequently, only its interaction with the two surfaces was considered. Fig. 9 and S5 show that UDMH preferentially adsorbs at bridge sites on both manganese oxides, yet

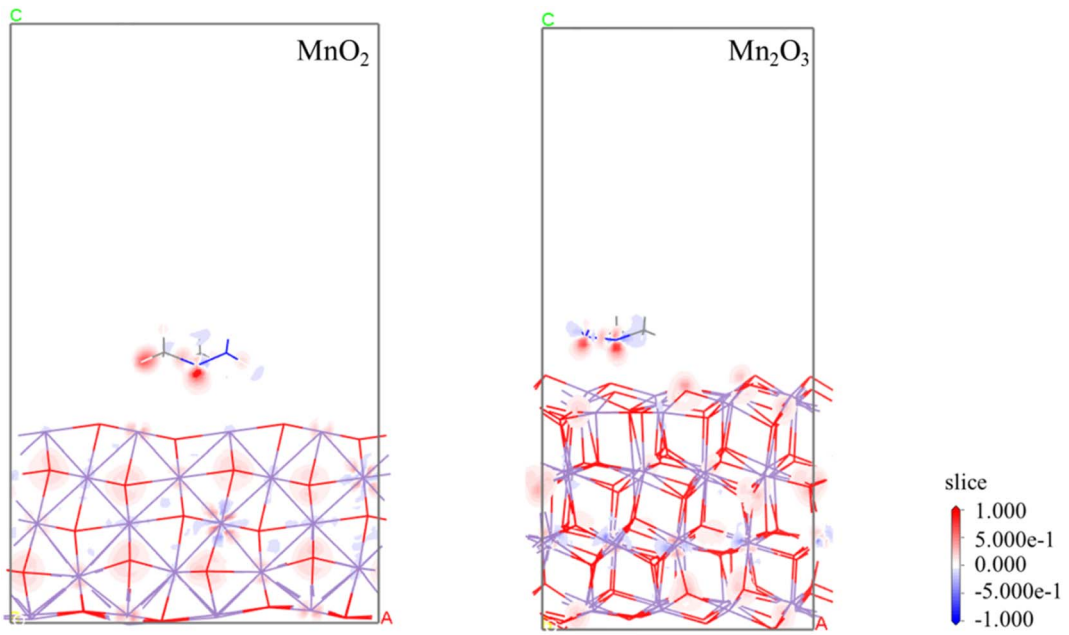

Fig. 10 Electron density difference diagram of UDMH adsorption on the MnO_2 (102) and Mn_2O_3 (2220) surfaces. (O atoms are red; N atom is blue; Mn atoms are gray; and blue and red indicate a decrease and increase in the electron density, respectively).

Table 4 Energies for UDMH adsorption on MnO_2 (102) and Mn_2O_3 (222) surfaces

Adsorption site	E_{ads} (kJ mol^{-1})	Adsorption distance (Å)
MnO_2	−88.77	2.99
Mn_2O_3	−13.51	3.59

with substantially disparate binding strengths. On MnO_2(102), the N–Mn adsorption distance is 2.99 Å and the adsorption energy is 88.77 kJ mol^{-1} (0.92 eV), placing the adduct in the weak chemisorption regime. In contrast, on Mn_2O_3 (222), the N–Mn separation is 3.59 Å, and the adsorption energy is only 13.51 kJ mol^{-1} (0.14 eV), indicative of pure van der Waals physisorption. Two-dimensional electron-density-difference maps sliced along the N–N bond and perpendicular to the surface (Fig. 10) reveal a pronounced electron-depletion zone (blue) on the Mn atom below nitrogen for MnO_2, whereas no appreciable charge transfer is detected on Mn_2O_3, consistent with the observed difference in adsorption strength (Table 4).

Kinetic analysis (Fig. 5) and SPME-GC-MS detection (Fig. S2–S3 and Table S4) outline the UDMH degradation pathway (Fig. 11), where intermediate concentrations peak at 5 min and stabilize after 60 min, validating the selected reaction duration.

Key differences emerge in intermediate conversion: both catalysts follow pathway ① to form tetramethyl tetrazene (TMT) and nitrosodimethylamine (NDMA) *via* radical recombination, but Pathway ② exhibits catalyst-specific behavior. MnO_2 promotes direct hydrogenation of critical intermediates to dimethylamine, enabling deep mineralization with over 90% COD removal and suppressing toxic byproducts. In contrast, Mn_2O_3 drives hydroxylation to formamide and favors the accumulation of highly methylated products, such as pentamethylpyrrole, which is attributed to its metallic electronic structure.

Combining XPS, XRD, radical quenching experiments, and DFT calculations, this study reveals that the degradation

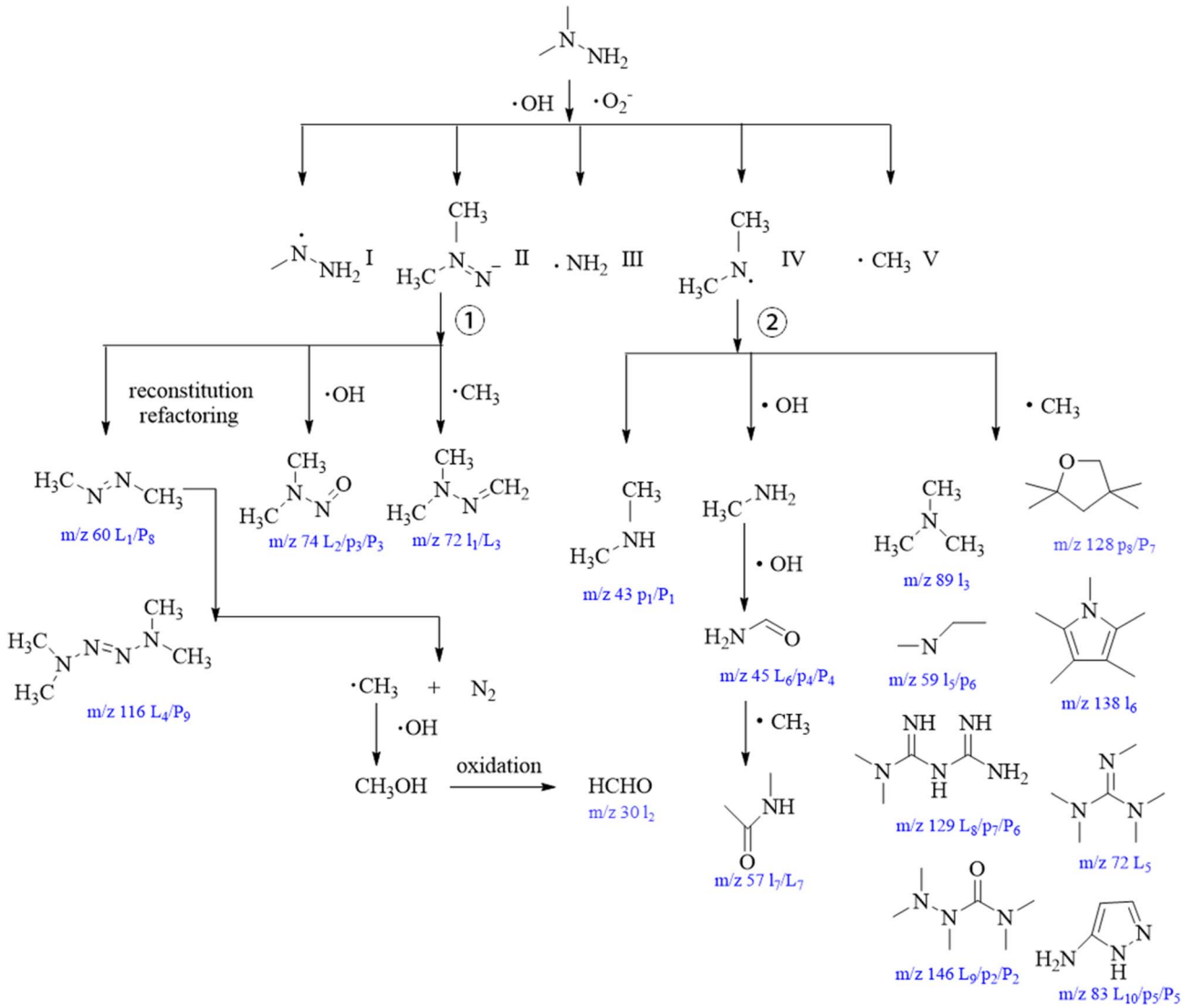

Fig. 11 UDMH degradation pathways in the microwave-assisted catalytic oxidation process. (For Mn_2O_3 degradation products, lowercase symbols (l_x) represent intermediates at 5 min, while uppercase symbols (L_x) denote products at 60 min. For MnO_2 degradation products, lowercase symbols (p_x) indicate intermediates at 5 min, and uppercase symbols (P_x) signify final products at 60 min.).

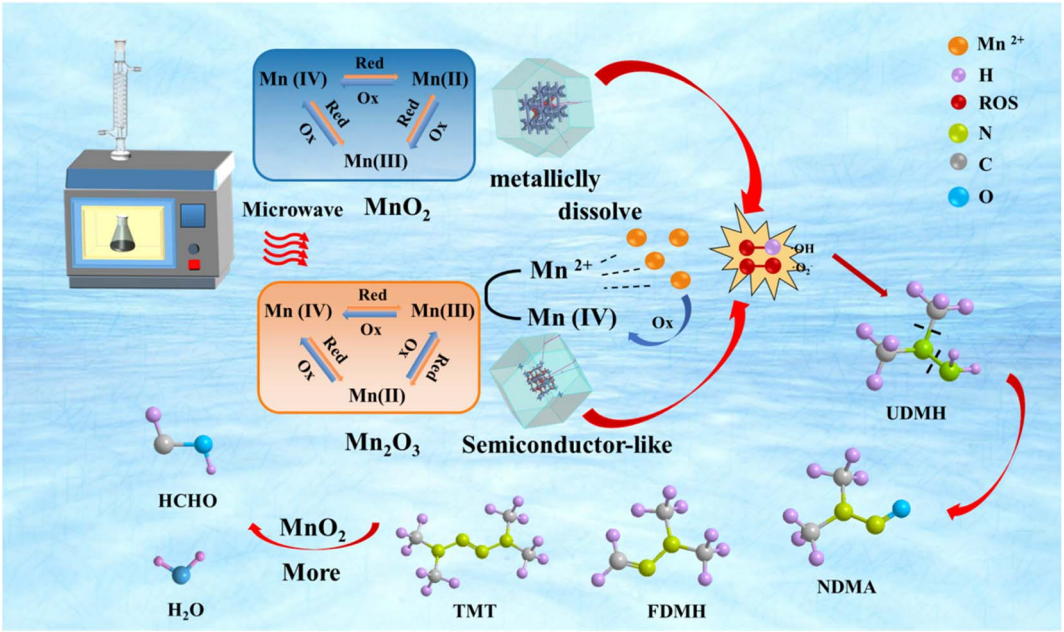

Fig. 12 Schematic of the UDMH degradation mechanisms.

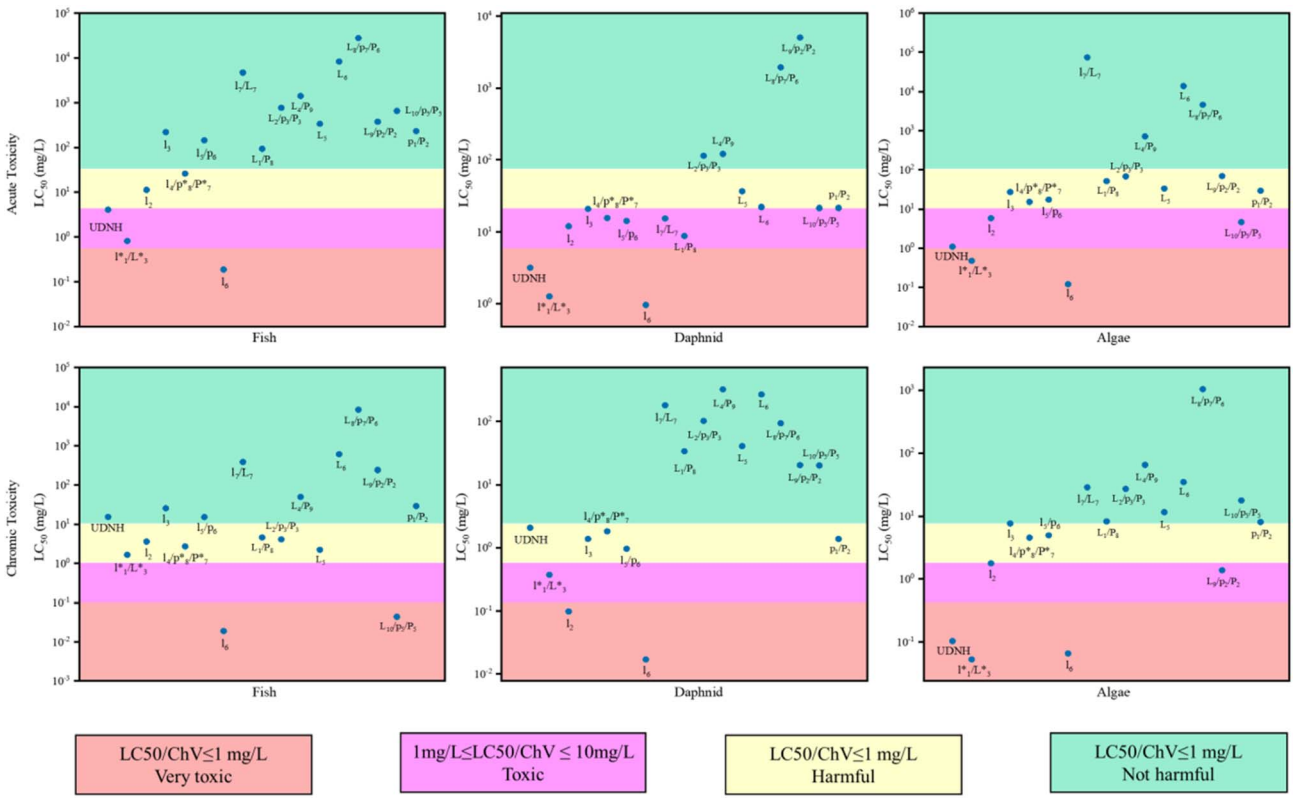

Fig. 13 Toxicity analysis results using ECOSAR software (for Mn_2O_3 degradation products, lowercase symbols (l_x) represent intermediates at 5 min, while uppercase symbols (L_x) denote products at 60 min. For MnO_2 degradation products, lowercase symbols (p_x) indicate intermediates at 5 min, and uppercase symbols (P_x) signify final products at 60 min).

mechanisms of UDMH in microwave-assisted manganese oxide systems exhibit significant valence-state dependency and catalyst specificity (Fig. 12). XPS analysis shows the changes in the ratio of $Mn^{2+}/Mn^{3+}/Mn^{4+}$ on the surfaces of MnO_2 and Mn_2O_3, confirming the differences in electron transfer pathways between the two under microwave fields. Benefiting from its low

oxygen-vacancy formation energy, MnO_2 facilitates the generation of $^{\cdot}OH$ *via* surface Mn^{4+} and hydroxyl oxygen, concomitantly producing Mn^{2+} and Mn^{3+} (eqn (1)). These radicals synergistically cleave the N–N and C–N bonds in UDMH, producing intermediates such as FDMH and NDMA, which are ultimately mineralized into CO_2 and H_2O. Furthermore, organic intermediates act as electron acceptors to drive the catalytic recycling of Mn^{2+} and Mn^{3+} to Mn^{4+} (eqn (2)), ensuring sustained catalytic activity. Owing to its metallic nature, Mn_2O_3 generates $^{\cdot}OH$ not only through a heterogeneous catalytic system[55] but also *via* dielectric heating loss and Mn^{3+} disproportionation reactions (eqn (3) and (4)). However, its low electron mobility results in insufficient radical generation efficiency, leading to the accumulation of toxic intermediates such as NDMA. Additionally, the accumulation of Mn^{2+} (0.27%) inhibits catalytic recycling, necessitating microwave-induced dipolar polarization to promote the re-oxidation of Mn^{2+}.

$$\equiv Mn^{4+} + OH^- \xrightarrow{\text{Microwave}} \equiv Mn^{2+} + \equiv Mn^{3+} + \cdot OH \quad (1)$$

$$\text{Organic[Ox]} + \equiv Mn^{2+} + \equiv Mn^{3+} \xrightarrow{\text{Microwave}} \text{Organic[Red]} + \equiv Mn^{4+} \quad (2)$$

$$3 \equiv Mn^{3+} \xrightarrow{\text{Microwave}} 2 \equiv Mn^{4+} + \equiv Mn^{2+} + Mn^{2+} \quad (3)$$

$$\equiv Mn^{2+} + Mn^{2+} + \text{Organic[Ox]} + O_2 + H_2O \xrightarrow{\text{Microwave}} \equiv Mn^{3+} + \equiv Mn^{4+} + \cdot OH \quad (4)$$

Finally, the ecotoxicological impacts of UDMH and its degradation products on three trophic levels were assessed using the ECOSAR predictive model. As shown in Fig. 13, acute toxicity was partially attenuated after 5 min of degradation. With the exception of intermediates l_1^*/L_3^* and l_6, all identified species exhibited reduced acute toxicity relative to the parent compound. The elevated toxicity of l_1^*/L_3^* and l_6 is attributed to the formation of C=N and conjugated C=C functionalities, respectively, which confer potent electrophilic character. Electrophilic reaction species (RES) can undergo nucleophilic attack on biomacromolecules—including proteins, nucleic acids, and lipids—eliciting adverse biological effects. Concurrently, chronic toxicity to algae decreased after 5 min, whereas hazard profiles for fish and daphnia intensified, presumably reflecting the higher protein content in these organisms and consequent susceptibility to electrophilic adduction.[56] Notably, following 60 min of treatment, the majority of degradation products exhibited toxicity levels substantially below that of UDMH. These results demonstrate that microwave-assisted catalysis achieves effective detoxification, despite the transient generation of high-toxicity intermediates.

Based on the experimental results, characterization analyses and theoretical calculations provided above, a microwave–driven reaction mechanism is proposed for catalytic performance comparison between MnO_2 and Mn_2O_3. MnO_2 excels in mineralization due to its low oxygen-vacancy formation energy, enriched surface hydroxyls, and stable Mn^{4+}, which confer superior stability (leaching < 0.02%) and efficient catalysis. In contrast, Mn_2O_3—although intrinsically metallic—suffers from a higher vacancy-formation penalty and pronounced Mn^{3+} disproportionation, causing incomplete nitrogen removal and intermediate accumulation, requiring post-treatment (*e.g.*, ozonation) to reduce NDMA risks.

4 Conclusion

This study reveals the mechanistic differences in the catalytic degradation of UDMH with MnO_2 and Mn_2O_3 under microwave-assisted conditions by comparing the relationship between the electronic structure, surface chemical behavior, and degradation performance of the two manganese oxides. The results show that, by its low oxygen-vacancy formation energy and dynamic $Mn^{2+}/Mn^{3+}/Mn^{4+}$ valence state cycle, MnO_2 efficiently generates $^{\cdot}OH$ through a heterogeneous surface oxidation pathway. This significantly improves the deep mineralization efficiency of UDMH (with a COD removal rate of >90%) and suppresses the formation of nitrosamine intermediates. On the other hand, due to the disproportionation reaction of Mn^{3+} in Mn_2O_3 ($2Mn^{3+} \rightarrow Mn^{2+} + Mn^{4+}$), a homogeneous-heterogeneous synergistic catalytic pathway is triggered, leading to the accumulation of formaldehyde and polymethylated products (such as pentamethylpyrrole and NDMA), which pose a higher toxicity risk. In addition, the enrichment of surface hydroxyl oxygen in MnO_2 and its self-cleaning properties endow it with excellent structural stability, while the loss of active components in Mn_2O_3 (with a leaching rate of 0.27%) limits its long-term performance. Therefore, MnO_2 is suitable for the deep mineralization of high-concentration wastewater, while Mn_2O_3 requires subsequent processes to control the risks associated with the intermediates. Future research can focus on the regulation of the surface nanostructures of manganese oxides to further enhance the selective degradation ability and the potential for engineering applications. This study provides a theoretical basis for the selection and optimization of manganese-based catalysts in the treatment of nitrogen-containing wastewater.

Author contributions

Jiepeng Wang: investigation, methodology, data curation, visualization, writing – original draft. Siyu He: investigation, writing – review & editing. Zhe Wang: investigation. Yunlong Deng: methodology. Jielei Hao: visualization. Xuqian Wang: investigation, methodology, writing – review & editing. Yongkui Zhang: conceptualization, methodology, supervision.

Conflicts of interest

The authors declare that they have no known competing financial interests or personal relationships that could have appeared to influence the work reported in this paper.

Data availability

All raw data and supporting information are provided in the supplementary information (SI). Supplementary information: detailed characterization methods and experimental procedures; supplementary XRD and XPS data; GC-MS analysis results; additional DFT calculation results; possible degradation products; and physicochemical data for MnO_2 and Mn_2O_3. See DOI: https://doi.org/10.1039/d6ra00930a.

Acknowledgements

The authors gratefully acknowledge funding support from the National Natural Science Foundation of China under grant No. 22178237 and the China Postdoctoral Science Foundation (funded Project No. 2023M742452). We also thank the Center of Engineering Experimental Teaching, School of Chemical Engineering, Sichuan University, for the technical support and acknowledge the kind assistance of Lin Xiang in ICP-OES quantitative analysis.

References

1 A. L. Milyushkin and A. E. Karnaeva, *Sci. Total Environ.*, 2023, **891**, 164367.
2 C. Hu, Y. Zhang, Y. Zhou, Z.-f. Liu and X.-s. Feng, *J. Hazard. Mater.*, 2022, **432**, 128708.
3 A. R. Zarei, A. Pedram and H. Rezaeivahidian, *Desalin. Water Treat.*, 2016, **57**, 18906–18914.
4 J. Su, J. Ying, H. Ruomeng, H. Yuanzheng, S. Keke and Z. and Hao, *Environ. Technol.*, 2023, **44**, 1493–1504.
5 Y. Hajizadeh, M. M. Amin, K. Ebrahim and I. Parseh, *Atmos. Pollut. Res.*, 2018, **9**, 37–46.
6 Q. L. Liao, C. G. Feng and L. Wang, *Appl. Sci.-Basel*, 2016, **6**, 19.
7 X. Zhang, Z. Guo, P. Sun, X. Liu, Z. Luo, J. Li, D. Zhang and X. Xu, *Sep. Purif. Technol.*, 2023, **312**, 123425.
8 Y. Z. Huang, Y. Jia, R. M. Hou, Z. Y. Huang, K. K. Shen, G. F. Jin and L. Hou, *RSC Adv.*, 2021, **11**, 24172–24182.
9 G. Prasannamedha and P. S. Kumar, *J. Clean Prod.*, 2020, **250**, 15.
10 X. Mu, W. Xuanjun, Z. Yue, L. Bo and J. Yang, *Environ. Technol.*, 2021, **42**, 2709–2720.
11 Y. Huang, Y. Jia, L. Zuo, Y. Huo, R. Liu and L. a. Hou, *Chem. Eng. J.*, 2022, **450**, 138054.
12 D. S. Kosyakov, N. V. Ul'yanovskii, I. I. Pikovskoi, B. Kenessov, N. V. Bakaikina, Z. Zhubatov and A. T. Lebedev, *Chemosphere*, 2019, **228**, 335–344.
13 S. Chandra, P. Das, S. Bag, R. Bhar and P. Pramanik, *Mater. Sci. Eng. B-Adv. Funct. Solid-State Mater.*, 2012, **177**, 855–861.
14 V. Alwera, S. Singh, V. C. Srivastava and T. K. Mandal, *ChemistrySelect*, 2020, **5**, 4674–4684.
15 C. D. Qi, X. T. Liu, C. Y. Lin, X. H. Zhang, J. Ma, H. B. Tan and W. Ye, *Chem. Eng. J.*, 2014, **249**, 6–14.
16 S. Sharma, T. Sharma, S. Pandey, S. Azizov and D. Kumar, in *Nanoparticles in Green Organic Synthesis*, ed. S. Bhunia, B. Kumar, P. Singh, R. Oraon and K.-H. Kim, Elsevier, 2023, pp. 241–253, DOI: 10.1016/B978-0-323-95921-6.00004-4.
17 W. Wang, F. Zhang, P. Chang, X. Luo, K. Miao and G. Feng, *Inorg. Chem. Commun.*, 2022, **143**, 109738.
18 L. Tian, G. Lv, L. Wu, L. Bian, M. Liu and L. Liao, *Appl. Surf. Sci.*, 2023, **621**, 156801.
19 T.-L. Lai, C.-C. Lee, K.-S. Wu, Y.-Y. Shu and C.-B. Wang, *Appl. Catal. B-Environ.*, 2006, **68**, 147–153.
20 I. Ibrahim, A. Kaltzoglou, C. Athanasekou, F. Katsaros, E. Devlin, A. G. Kontos, N. Ioannidis, M. Perraki, P. Tsakiridis, L. Sygellou, M. Antoniadou and P. Falaras, *Chem. Eng. J.*, 2020, **381**, 12.
21 C. Yin, J. J. Cai, L. F. Gao, J. Y. Yin and J. C. Zhou, *J. Hazard. Mater.*, 2016, **305**, 15–20.
22 Y. H. Zhou, X. X. Lei, J. Y. Zhou, D. L. Yan, B. Deng, Y. D. Liu and W. L. Xu, *Catal. Surv. Asia*, 2023, **27**, 319–331.
23 P. Wang, J. Zhao, Q. Zhao, X. Ma, X. Du, X. Hao, B. Tang, A. Abudula and G. Guan, *J. Colloid Interface Sci.*, 2022, **607**, 100–110.
24 Y. Gao and D. L. Zou, *Chem. Eng. J.*, 2020, **393**, 11.
25 E. R. Stobbe, B. A. de Boer and J. W. Geus, *Catal. Today*, 1999, **47**, 161–167.
26 S.-L. Chiam, S.-Y. Pung, F. Y. Yeoh and M. Ahmadipour, *Mater. Chem. Phys.*, 2022, **280**, 125848.
27 X. Zhang, X. Zhang, B. Zhou, P. Wang, Y. Wang, F. Meng, C. Wei, X. Huang and G. Wen, *Colloids Surf., A*, 2023, **667**, 131436.
28 C. Yin, J. Cai, L. Gao, J. Yin and J. Zhou, *J. Hazard. Mater.*, 2016, **305**, 15–20.
29 I. Ibrahim, A. Kaltzoglou, C. Athanasekou, F. Katsaros, E. Devlin, A. G. Kontos, N. Ioannidis, M. Perraki, P. Tsakiridis, L. Sygellou, M. Antoniadou and P. Falaras, *Chem. Eng. J.*, 2020, **381**, 122730.
30 J. Yan, L. Han, W. Gao, S. Xue and M. Chen, *Bioresour. Technol.*, 2015, **175**, 269–274.
31 F. Wang, T. Li, Y. Fang, Z. Wang and J. Zhu, *J. Alloy. Compd.*, 2021, **857**, 157531.
32 Y. Wang, X. Li, J. Xiao, D. Chen, N. Li, Q. Xu, H. Li, J. He and J. Lu, *Sci. Total Environ.*, 2022, **839**, 156345.
33 K. Li, H. Li, T. Xiao, J. Long, G. Zhang, Y. Li, X. Liu, Z. Liang, F. Zheng and P. Zhang, *J. Environ. Manage.*, 2019, **251**, 109563.
34 L. Yang, F. Yang, H. Zhang, H. Zhou, M. Luo, Y. Liu, C. Zhao, L. Zheng and B. Lai, *J. Hazard. Mater.*, 2023, **454**, 131479.
35 H. Yan, S. Yao, J. Wang, S. Zhao, Y. Sun, M. Liu, X. Zhou, G. Zhang, X. Jin, X. Feng, Y. Liu, X. Chen, D. Chen and C. Yang, *Appl. Catal. B-Environ.*, 2021, **284**, 119803.
36 Y. Li, J. You, Z. Yu, C. Du, Y. Wang and S. Cheng, *Int. J. Electrochem. Sci.*, 2024, **19**, 100663.
37 D. Jia, M. Brigante, C. Zhang and G. Mailhot, *J. Water Process. Eng.*, 2023, **56**, 104388.
38 X. Liu, X. Yan, W. Liu, Q. Yan and M. Xing, *Sci. Bull.*, 2023, **68**, 603–612.
39 G. Huang, Y. Zhou, J. Zhang, W. He, X. Zeng, D. Feng, Y. Ge and Y. Shao, *ChemistrySelect*, 2024, **9**, e202404504.
40 J. K. Klewicki, *The Kinetics of Redox Reactions of Mn(II) and Mn(III) in Aqueous Systems: Homogeneous Autoxidation of*

Mn(II) and the Formation and Disappearance of Mn(III) Complexes, PhD thesis, California Institute of Technology, 1996.
41 L. Zhang, J. Ma and M. Yu, *Solid State Sci.*, 2008, **10**, 148–153.
42 A. A. Yousef, M. A. Arafa and M. A. Malati, *Open J. Appl. Chem. Biotechnol.*, 2007, **21**, 200–207.
43 H. Liu, X. Cui, X. Lu, E. D. Flynn and J. G. Catalano, *Geochim. Cosmochim. Acta*, 2025, **395**, 166–180.
44 J. Wang, H. Tang, H. Ren, R. Yu, J. Qi, D. Mao, H. Zhao and D. Wang, *Advanced Science*, 2014, **1**, 1400011.
45 P. Liu, Z. Wu, A. V. Abramova and G. Cravotto, *Ultrason. Sonochem.*, 2021, **74**, 105566.
46 M. Rabe, C. Toparli, Y.-H. Chen, O. Kasian, K. J. J. Mayrhofer and A. Erbe, *Phys. Chem. Chem. Phys.*, 2019, **21**, 10457–10469.
47 S. Wang, Y. x. Wang, J. Wang, Z. Jiang, J. Ma, Y. Liu, Y. Zhou, Z. Zhang and C. Chen, *ACS ES&T Engineering*, 2025, DOI: 10.1021/acsestengg.5c00021.
48 Y. Z. Huang, Y. Jia, L. Zuo, Y. G. Huo, R. Y. Liu and L. A. Hou, *Chem. Eng. J.*, 2022, **450**, 12.
49 Y. Z. Huang, Y. Jia, L. Zuo, Y. G. Huo, Y. Y. Zhang and L. Hou, *J. Water Process. Eng.*, 2022, **49**, 9.
50 Y. Zhang, Q. Li, Q. Gao, S. Wan, P. Yao and X. Zhu, *Appl. Catal. B-Environ.*, 2020, **267**, 118715.
51 J. Wang, Y. Zhou, Y. Shao, F. He, M. Wu, H. Ni, Y. Zheng and Y. Sun, *Res. Chem. Intermed.*, 2019, **45**, 1721–1735.
52 L. Yi, L. Guo, H. Jin, J. Kou, D. Zhang and R. Wang, *Int. J. Hydrogen Energy*, 2018, **43**, 8644–8654.
53 Y. Hajizadeh, M.-M. Amin, K. Ebrahim and I. Parseh, *Atmos. Pollut. Res.*, 2018, **9**, 37–46.
54 F.-X. Tian, H. Li, M. Zhu, W. Tu, D. Lin and Y.-F. Han, *ACS Appl. Mater. Interfaces*, 2022, **14**, 18525–18538.
55 J. Wang, W. Tong, X. Wang, P. Li, H. Yan and Y. Zhang, *Sep. Purif. Technol.*, 2023, **327**, 124849.
56 S. J. Enoch and M. T. Cronin, *Crit. Rev. Toxicol.*, 2010, **40**, 728–748.